Organic Electronics Hot Paper

How to cite: *Angew. Chem. Int. Ed.* **2022,** *61,* e202209726
International Edition: doi.org/10.1002/anie.202209726
German Edition: doi.org/10.1002/ange.202209726

Open-Bandgap Graphene-Based Field-Effect Transistor Using Oligo(phenylene-ethynylene) Interfacial Chemistry

*Kyung Ho Kim[+], Sung Eun Seo[+], Chul Soon Park, Soomin Kim, Soohyun Lee, Choong-Min Ryu, Dongeun Yong, Yoo Min Park, and Oh Seok Kwon**

Abstract: Organic interfacial compounds (OICs) are required as linkers for the highly stable and efficient immobilization of bioprobes in nanobiosensors using 2D nanomaterials such as graphene. Herein, we first demonstrated the fabrication of a field-effect transistor (FET) via a microelectromechanical system process after covalent functionalization on large-scale graphene by introducing oligo(phenylene-ethynylene)amine (OPE). OPE was compared to various OICs by density functional theory simulations and was confirmed to have a higher binding energy with graphene and a lower band gap than other OICs. OPE can improve the immobilization efficiency of a bioprobe by forming a self-assembly monolayer via anion-based reaction. Using this technology, Magainin I-conjugated OGMFET (MOGMFET) showed a high sensitivity, high selectivity, with a limit of detection of 10^0 cfu mL^{-1}. These results indicate that the OPE OIC can be applied for stable and comfortable interfacing technology for biosensor fabrication.

[*] K. H. Kim,[+] S. E. Seo,[+] Dr. C. S. Park, S. Kim, S. Lee, Dr. C.-M. Ryu, Dr. O. S. Kwon
Infectious Disease Research Center, Korea Research Institute of Bioscience and Biotechnology (KRIBB)
Daejeon 34141 (Republic of Korea)
E-mail: oskwon79@kribb.re.kr

Prof. D. Yong
Department of Laboratory Medicine and Research Institute of Bacterial Resistance, Yonsei University College of Medicine
Seoul (Republic of Korea)

Dr. Y. M. Park
Division of Nano-Bio Sensors/Chips Development,
National NanoFab Center (NNFC)
Daejeon (Republic of Korea)

Dr. O. S. Kwon
College of Biotechnology and Bioengineering,
Sungkyunkwan University
Suwon 16419 (Republic of Korea)

[+] These authors contributed equally

© 2022 The Authors. Angewandte Chemie International Edition published by Wiley-VCH GmbH. This is an open access article under the terms of the Creative Commons Attribution Non-Commercial License, which permits use, distribution and reproduction in any medium, provided the original work is properly cited and is not used for commercial purposes.

Introduction

In recent years, nanomaterials have been used for nanotechnology and have been developed with various shapes and sizes, such as nanoparticles, nanotubes, nanowires, nanorods, and nanosheets. These materials have been utilized for the development of the sensor platform due to their excellent electrical properties.[1] Among the conducting nanomaterials, graphene is a two-dimensional (2D) carbon nanomaterial with a zero band gap, sp^2-hybridized carbon atoms, and a carbon network with unprecedented properties, including extraordinary mechanical stiffness, strength, and elasticity; outstanding electrical and thermal conductivity; and many others.[2–7] Recently, graphene was used for the development of a biosensor platform, and graphene-based biosensors were developed for the detection and monitoring of various markers, such as bacteria, viruses, organisms, antibodies, antigens, and biomolecules. In this system, organic interfacial chemicals (OICs) were required for the immobilization of the bioprobe. Although many OICs, such as π-interaction molecules, free radical derivatives, carbene, nitrene, and aryne have been developed and utilized for conjugation onto graphene surfaces, π-interaction-based conjugation materials are mostly used as linker compounds for the fabrication of biosensor platforms. However, these OICs have a lower interaction energy than covalent bond-based OICs. In addition, a field-effect transistor (FET) of the biosensor platform was fabricated by using a microelectromechanical systems (MEMS), and many energies, such as the thermal energy, vacuum energy, physical energy, and sound energy, were required for the MEMS process. Therefore, the introduction of OICs onto the graphene surface progressed after the MEMS process ended.[8–13] The conjugation efficiency of OIC interfacial compounds onto graphene and the introduction efficiency of the bioprobe are limited owing to steric hinderance or the amount of the activated functional group.[14] Therefore, OICs are required to have self-assembly, highly stable interactions, and high immobilization efficiency, and the preparation of covalent bond-based OICs is still challenging due to the need for molecular design with terminal functional groups and new patterning technologies.[15]

In this study, the oligo(phenylene-ethynylene) (OPE) interfacial compound was designed by functionalization of the amine group at the terminus. A self-assembly monolayer (SAM) was formed by anion-based reaction of the OPE with graphene micropatterned (GM) hybridized carbon atoms.[16] The synthesized OPE was compared with OICs,

 © 2022 The Authors. Angewandte Chemie International Edition published by Wiley-VCH GmbH

and the interaction energy and binding stability with GM were determined by performing density functional theory (DFT) simulations. Based on the results, OPE was theoretically confirmed to be a more stable state with a high interaction energy over 700 times, and electron transfer from OPE to GM was observed by analyzing the electron density difference map (EDDM).[17] The opening of the band gap was confirmed to occur by covalent bonding between GM and OPE based on the calculated orbital energy gap (OEG).[18] Moreover, the NH_2-functionalized OPE compound has the advantage of an easier two-step synthesis process, with interactions with graphene by anion-based reaction. OPE-based GM (OGM) side-gate system electrodes were fabricated using a microelectromechanical system (MEMS), and the properties of the OPE-conjugated large-scale graphene and OGM were determined using, spectroscopy, optical, and electronic analyses. Magainin I-conjugated OGM (MOGM) was fabricated as a biosensor for application in bacteria detection, and the properties and real-time performance were determined to confirm the performance of monitoring as a MOGM field-effect transistor (MOGMFET). The MOGMFET exhibited high sensitivity, with a limit of detection (LOD) of 10^0 cfu mL^{-1}, and a high selectivity in Gram-negative bacteria. Based on the results, the OPE OIC was shown to be a suitable interfacial compound for biosensor fabrication.

Results and Discussion

The schematic illustration presents the whole fabrication process for the MOGMFET system involving covalent bonding onto large-scale graphene (Scheme 1). The OPE-based OIC was first conjugated onto nonpatterned large-scale graphene on a 4-inch wafer, and then the MEMS process was performed for fabrication of the side-gated OGMFET. Magainin I was conjugated with the amine group of the OPE terminus by amide bonding for the specific detection of Gram-negative bacteria, and MOGMFETs were developed. The MOGMFET was exposed to pre-treated clinical *E. coli*, and the electrical signal was monitored in real time.

Interfacing compounds were introduced to immobilize the bioprobe onto the GM surface, and various interfacial compounds, including diaminonaphthalene (DAN), 1-pyrenebutyric acid N-hydroxysuccinimide ester (PANHS), bis(2-aminoethylene)perylene-3,4,9,10-tetracarboxyldiimide-diacid (PDI) and bis(2-aminoethylene)perylene-3,4,9,10-tetracarboxyldiimide-diamine (PDA), participated in π stacking interactions between the aromatic ring backbone and graphene.[9,10,19–22] π-π interactions are a type of noncovalent interaction; therefore, the interaction energy is lower than that of covalent bonds. To investigate the interaction energy and the binding stability, the interacting 3D structures, electron density and binding energies were calculated via density functional theory (DFT) simulations (Figure 1). To investigate the interaction energy between each interfacial compound and GM, calculations were performed using the results obtained from DFT simulations. The absolute energy (ΔE_{abs}) of the interfacing compounds was −55195.4 eV for GM, −13248.2 eV for DAN, −34192.7 eV for PANHS, −42659.7 eV for PDA, −51865.7 eV for PDI and −670.350 eV for OPE (Table S1). Based on these results, the interaction net energy (ΔE_{int}) between GM and each

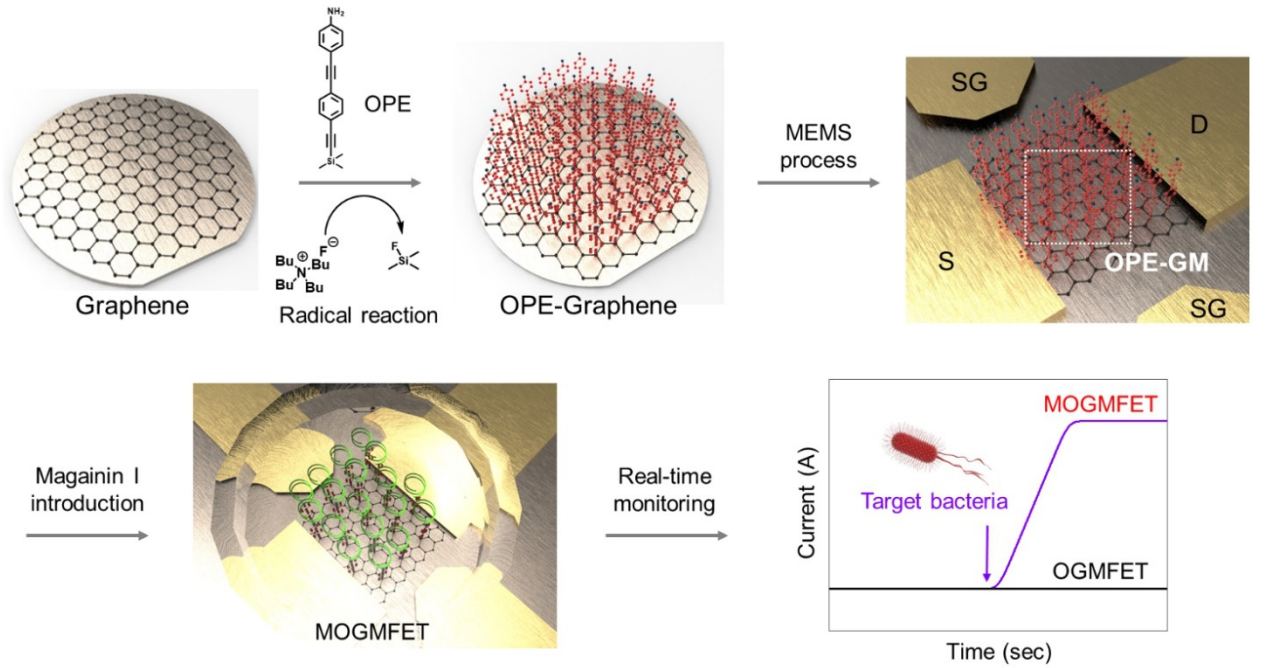

Scheme 1. Schematic diagram of the fabrication and monitoring of the MOGMFET system.

© 2022 The Authors. Angewandte Chemie International Edition published by Wiley-VCH GmbH

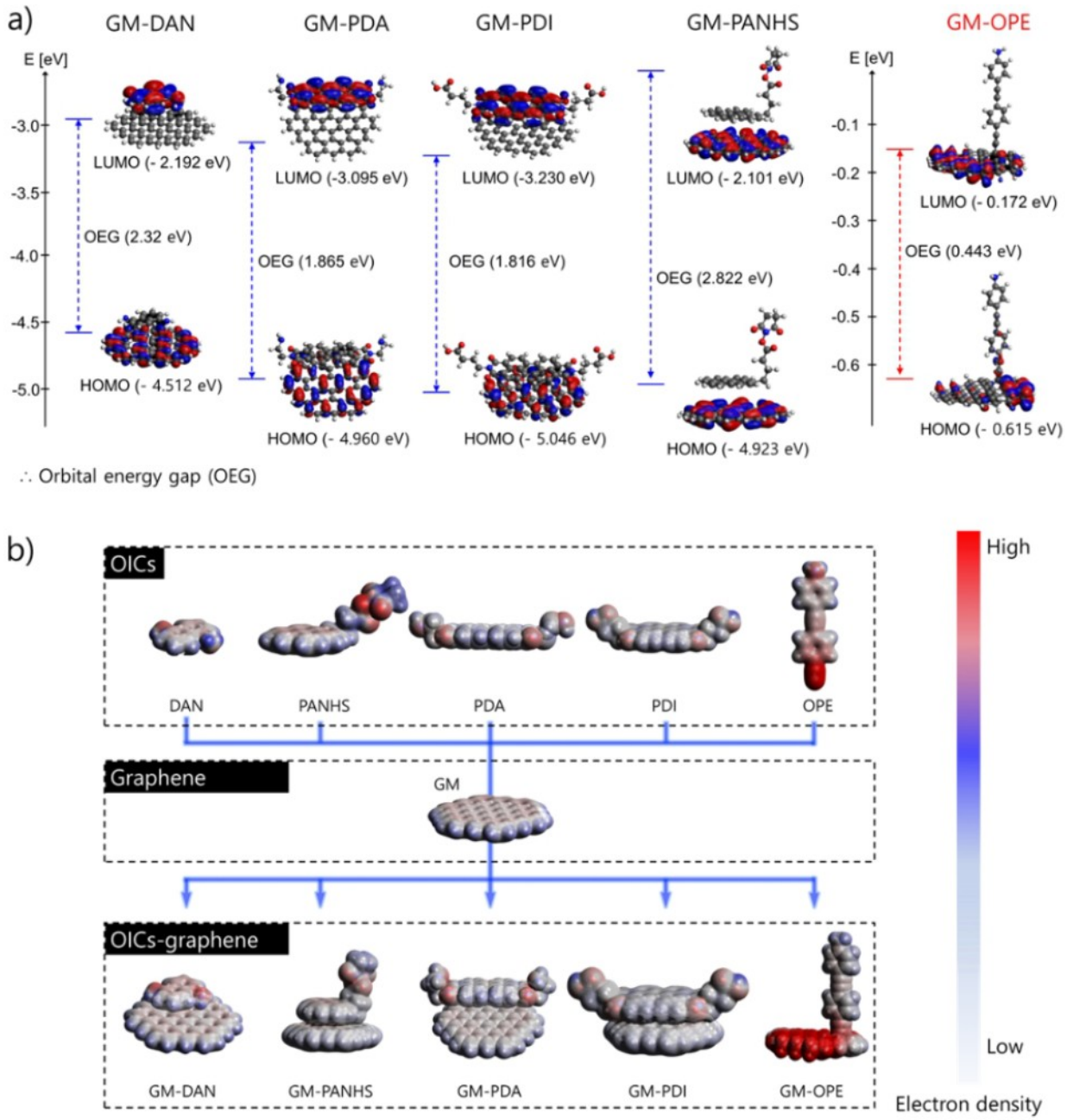

Figure 1. a) 3D structures of HOMO and LUMO and the orbital energy gap (OEG) depending on the DFT simulation results of each interfacial chemical: DAN, PDA, PDI, PANHS, and OPE. b) Electron density difference map (EDDM) (±0.001 a.u.) results before and after the interaction of each interfacial compound with GM.

interfacial chemical was calculated via the following equation [Eq. (1)].

$$\Delta E_{int} = E_b - [E_{GM} + E_{chem}] \quad (1)$$

where E_{GM}, E_{chem} and E_b indicate the absolute energy of each compound, including GM, and the interaction energy between graphene and the interfacing compounds. The calculated ΔE_{int} values were −0.0571 eV for DAN/GM, −0.24387 eV for PANHS/GM, −0.1239 eV for PDA/GM, −0.0708 eV for PDI/GM, and −89.7083 eV for OPE/GM. For those interfacial compounds, the ΔE_{int} of OPE was found to be higher than 700 times, indicating a stable interaction state.[23] The highest occupied molecular orbital (HOMO) and lowest unoccupied molecular orbital (LUMO) were investigated in the calculations of the OEG (the independent-particle gap).[24] The orbital energy gap was 2.32 eV for DAN/GM, 1.865 eV for PDA/GM, 2.822 eV for PANHS/GM, 1.816 eV for OEG-based band gap, which decreased by approximately 80 % compared to the average OEG of other OICs.[25] Therefore, gap-opened graphene by introducing OPE was tuned to be more attractive for FET

© 2022 The Authors. Angewandte Chemie International Edition published by Wiley-VCH GmbH

applications due to the increasing performance of electrical transport.[26] EDDM simulations were carried out to determine the electron dispersion (Figure 1b). The compounds inducing π interactions were observed by the distributed trend of the electron overall, whereas OPE exhibited a possible anion-based reaction site at the terminus (active site; orange circle). Moreover, after interaction with GM, only OPE showed electron movement to GM due to possible electron transfer by covalent bonding.[27,28]

The OPE compound containing a functional amine group was designed from DFT simulations, and the total synthesis scheme consisted of a simple step (Figure 2). The molecule was synthesized through the Sonogashira coupling reaction with a palladium catalyst and copper(I) catalyst, and NH_2-functionalized OPE was clearly confirmed by ^1H NMR analysis (Figure S1). The 4-(4-(trimethylsilylethynyl)-phenylethynyl)aniline compound can be easily obtained to form a trimethylsilyl protected intermediate product, which reacted with tetrabutylammonium fluoride (TBAF) to deprotect silyl ether groups under mild basic conditions. During deprotection of the trimethylsilyl group, the reaction of the OPE intermediate involved formation of an ethynyl anion, which is a strong base or strong nucleophile like an acetylide.[29] Accordingly, the ethynyl anion is capable of bonding to the 2D single layer graphene surface because of its powerful reactivity (Figure S2). The formation of the OPE layer was investigated by X-ray photoelectron spectroscopy (XPS), and the survey scan spectra displayed a set of core O 1s, N 1s, and C 1s spectra (Figure 3a). The specific C 1s peaks of the C=C sp^2 (284.7 eV), C–C sp^3 (285.6 eV), and π-π* satellites (291.1 eV) were observed by fitting the C 1s core level of pristine graphene, and deconvolution of the broad C 1s components of OPE-introduced graphene resulted in C≡C sp (283.5 eV), C=C sp^2 (284.0 eV), C–C sp^3 (284.9 eV), C–NH_2 (286.1 eV), and π-π* satellites (288.7 eV) (Figure S3). The newly sp-hybridized carbon peak appeared at 283.5 eV with a lower intensity.[30] The N 1s spectra were decomposed into two contributions, and the interpretation of the N 1s peak of the OPE revealed two representative peaks at 401.8 eV and 399.6 eV assigned to the NH_3^+ and NH_2 groups, respectively. (Figure 3b).[31] Evidence for the OPE-introduced graphene was provided by confirming the gradual shift toward lower binding energies than pristine graphene due to the amino functionalization on the terminus. Raman spectroscopy was performed to investigate the successful covalent bonding of OPE onto graphene, and the spectra indicated the introduction of the linear aromatic molecule on the graphene surface (Figure 3c). Pristine single-layer graphene showed a G peak (1584 cm^{-1}) and 2D peak (2638 cm^{-1}) due to the E_{2g} vibrational mode of sp^2-bonded carbon and a second-order vibration by the scattering of phonons at the zone boundary, respectively.[32–34] The intensity ratio of the 2D peak to the G peak (I_{2D}/I_G) showed ideal monolayer graphene (approximately 1.99). After covalent bonding by OPE, a change in the spectra was observed, with the appearance of the D band (1333 cm^{-1}) and decrease in the intensity of the 2D band. The generated D band indicates the A_{1g} mode breathing vibration of six-membered sp^2 carbon rings, and the neighboring sp^2 bonded carbons were changed to the sp^3 hybridized carbon of graphene.[35] The D band was integrated with the D* band (1625 cm^{-1}), and the D + D* band was observed at 2916 cm^{-1}. Although in the spectra of the OPE-functionalized graphene, there was no obvious band shift, the full width at half-maximum (FWHM) increased from 26 cm^{-1} of pristine graphene to 41 cm^{-1}.[36]

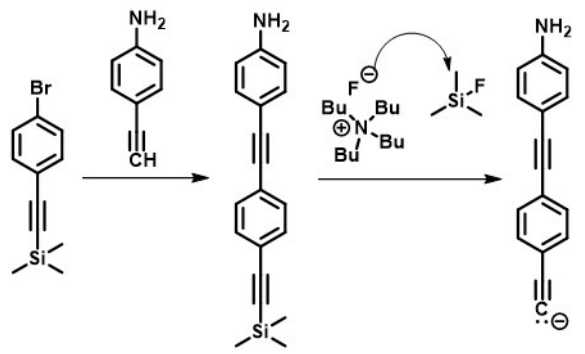

Figure 2. Synthesis schematic diagram of OPE OIC.

To investigate the topography, Cs-corrected high-resolution field emission-transmission electron microscopy (Cs-corrected FE-TEM) analysis was performed before and after OPE introduction on the graphene. For pristine graphene, the image exhibited perfect hexagonal patterns and a uniform hexagonal lattice, and (111) planes were observed in the selected area electron diffraction (SAED) image (Figures 3d, inset, and S4a). In particular, the observation of the (111) plane was significant owing to the covalent bonding of OPE on graphene.[16,37] After the introduction of OPE, the topography changed to different symmetrical patterns, including an aromatic ring in a vertical structure and an amine group at the terminus (Figure 3e). The additional diffraction patterns were confirmed to result from the surroundings of the graphene (111) plane (Figures 3e, inset, and S4b). Therefore, the covalent bonding between OPE and graphene was demonstrated by the SAED pattern image. The formation of uniform OPE SAMs was verified by the optical change of large surface morphology and hydrophilicity on the sample surface with the contact angle measurement (Figure 3f). The graphene surface showed a significant difference before ($\theta = 88.5°$) and after ($\theta = 60.5°$) surface coating. In particular, those parameters (four points each) over large areas showed similar hydrophilicity within the deviation of 5°. The hydrophilicity after OPE introduction was increased compared with that of pristine graphene due to the NH_2 functional group of the terminus OPE.

Fourier transform infrared (FT-IR) spectroscopy was performed to investigate NH_2-functionalized OPE conjugation on graphene. (Figure 3g). Several peaks attributed to nitrogen-containing functional groups appeared at 1284, 1616, 1230 to 1020, and 2210 cm^{-1}, corresponding to the N–H stretching vibration, N–H bending vibration, C–N stretching vibration, and C≡C stretching vibration, respectively.[38] However, in the spectra of the pristine graphene, the most dominant peaks were $=CH_2$ asymmetric and symmetric stretching at 2915 cm^{-1} and 2850 cm^{-1}.[39] The

© 2022 The Authors. Angewandte Chemie International Edition published by Wiley-VCH GmbH

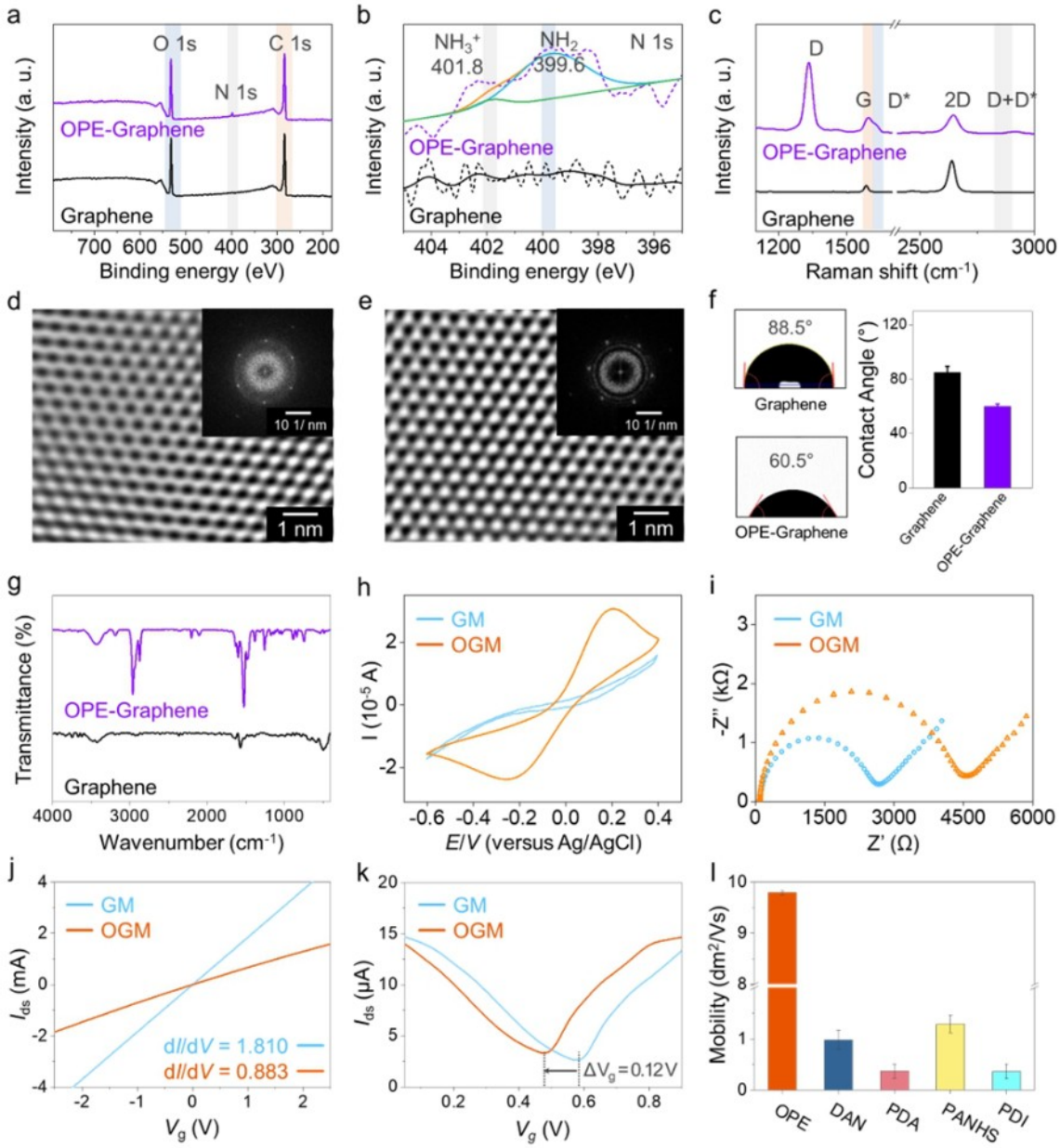

Figure 3. Characterization of graphene before and after OPE introduction. a,b) XPS survey and N 1s narrow spectra and c) Raman spectra depending on the OPE introduction. d,e) TEM and SAED images. f) AFM and contact angle (inset) images of the surface of pristine graphene and OPE-introduced graphene. g) FT-IR spectra. h) CV curves in 0.1 mM $NaClO_4$ solution at a scan rate of 0.1 V/s. i) Nyquist plots of OPE-NH_2-GM and the bare graphene loaded electrode obtained in the range from 0.05 Hz to 100 kHz at a representative potential of 0 V in 0.1 mM $NaClO_4$. The electrical properties j) *I–V* curves, k) transfer curves, l) carrier mobility through the Hall effect measurements toward each OIC.

stretching and bending vibrations of the C–H bond were observed at 833 cm^{-1} and 672 cm^{-1}, respectively. The peak at approximately 1519 cm^{-1} was attributed to C=C stretching from pristine graphene.

Cyclic voltammetry (CV) and electrochemical impedance spectroscopy (EIS) were performed to investigate the electrochemical properties, such as surface variances and impedance. The oxidation and reduction peaks were observed in 0.203 V and - 0.256 V due to the surface change depending on the covalent bonding of OPE OIC on the GM (Figure 3h). The density of covalent bonding was calculated by integration of the CV curve, and peaks were observed at 3.4876 mol nm^{-2} for oxidation and 3.8289 mol nm^{-2} for reduction. The semicircle was enlarged from pristine GM (1.369 kΩ) to OGM (1.863 kΩ), which indicates that the impedance responses (R_{ct}) in the surface change depend on OPE introduction (Figure 3i and S5). The current-voltage (*I–V*) curves showed the ohmic connection toward GM and OGM in the range of −2.5 to +2.5 V (Figure 3j). Although the slope (d*I*/d*V*) decreased from 1.810 to 0.883, which was the clear phenomenon of the introduction of OPE. The transfer curve measurements were carried out to investigate

© 2022 The Authors. Angewandte Chemie International Edition published by Wiley-VCH GmbH

the additional electrical properties (Figure 3k). The Dirac point was negatively shifted from 0.75 V (GM) to 0.65 V (OGM) owing to the n-doping effect by electron transfer based on the DFT simulation and EDDM. The carrier mobility toward each OIC was obtained by measuring the Hall effect, and the mobility of OPE/GM was highest at 0.9848, 0.3717, 0.3618, 1.293, and 9.799 $dm^2 Vs^{-1}$ for DAN/GM, PDA/GM, PDI/GM, PANHS/GM, and OGM, respectively (Figure 3l). Moreover, the Hall coefficient was higher at 325 $cm^3 C^{-1}$ than other OICs, and OGM showed the best electrical properties among the various OICs (Table S3). The results of the Hall effect measurements showed the excellent electrical properties of OGM. In addition, the hysteresis was measured to comparison the stability in FET system (PBS, pH 7.0) toward all OICs. OPE showed the lowest variance as 0.16 V of the shift of Dirac point (Figure S6). These results were the effect of covalent bonding and electron transfer.

Figure 4a presents the fabricated electrodes. The side-gated OGMFET was fabricated by 4-inch wafer-scale electrodes using the MEMS process. A side-gate was formed onto the coplanar with source/drain electrodes, and the channel consisted of the OPE conjugated-GM. To confirm the bonding of magainin I to the OGMFET terminus, the current-voltage (I–V) curve was measured to confirm the conductivity change in the range of −2 V to 2 V (Figure 4b). The curves appeared linear and were slightly decreased from 1.38 to 1.2 upon conjugation of magainin I with the amine group of the OPE terminus. Although the conductivity ($\Delta I/\Delta V$) was decreased by functionalization, the curves followed Ohm's law and maintained ohmic behavior.[20,40,41] Figure 4c illustrates the 3D structures and the amino acid sequence of magainin I for the specific detection of Gram-negative bacteria. In particular, the red circles indicate the specific binding site as cationic groups, such as Lys4, His7, Lys10, Lys11, and Lys14,

which interact with the negatively charged membrane of Gram-negative bacteria. Therefore, the sensing mechanism was based on the charge interaction due to having a net charge of magainin I being positively charged, and the membrane of *E. coli* was formed and killed by AMP interaction.[42–44] The schematic illustration displays the magainin I-conjugated side-gated OGMFET (MOGMFET). The system consisted of source/drain and coplanar side-gate electrodes for supplying the voltage (Figure 4d). The chamber was placed on the channel and was immersed using PBS pH 7.4 as a dielectric. The formation of a field effect by supplying the gate voltage was supported and promoted from a dielectric material. The output curves (I_{ds}–V_{ds}) were obtained by varying the gate voltage, which was observed to have the p-type property of negatively increasing the current following a negative increase in the gate voltage range of 0.2 V to −1 V, as shown in Figure 4e. These results indicated that the charge carrier was based on the hole and exhibited the p-type characteristic transistor, which was a suitable platform for biosensor applications. In particular, n-type transistors cannot be utilized for biosensors due to the occurrence of damage to biomolecules by radicals.[45] The transfer curves indicated the charge density and the movement of the Dirac point (Figure 4f). The OGMFET displayed a Dirac point at 0.35 V, while the Dirac point was negatively shifted to 0.15 V ($\Delta V_g = -0.2$ V) after magainin I conjugation due to the positive charge of magainin I. These results indicate that the doping effect depends on the obvious immobilization via amide bonds onto the OGMFET of the bioreceptor.[46]

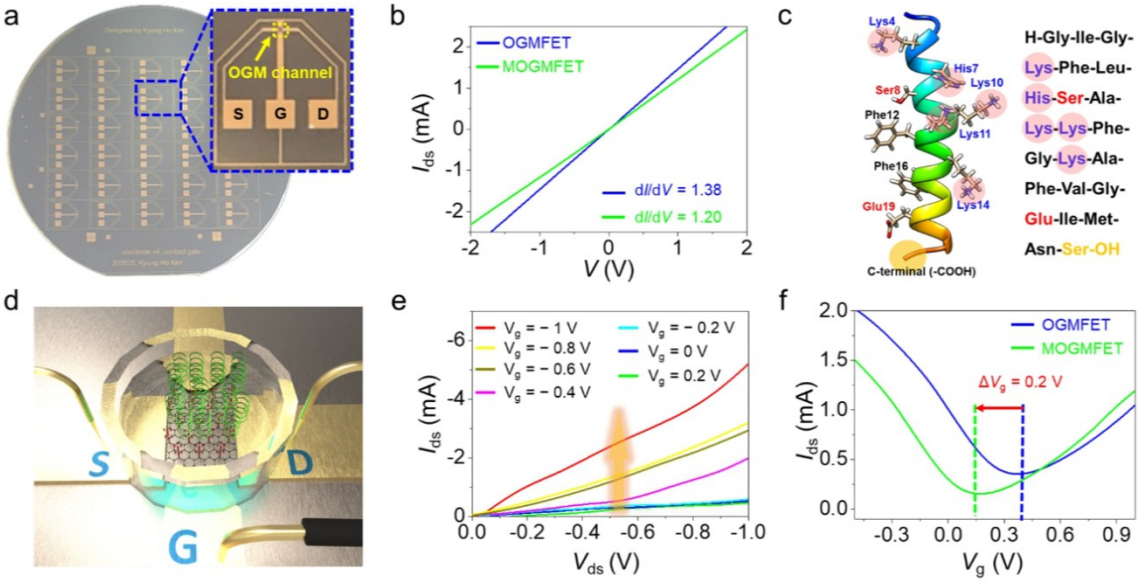

Figure 4. a) Optical image of the fabricated electrode from OPE-conjugated large-scale graphene. b) I–V curve before and after magainin I was introduced into the OGMFET. c) 3D structure and sequence of magainin I. d) Schematic illustration of the MOGMFET based on the side-gate system, which consisted of a source/drain and side-gate. e) Output curves of the MOGMFET depending on various gate voltage ranges of $V_g = -1$ to 0.2 V ($V_{ds} = 0$ to −0.5). f) Transfer curve change depending on the magainin I introduction ($V_{ds} = -10$ mV).

© 2022 The Authors. Angewandte Chemie International Edition published by Wiley-VCH GmbH

The illustration scheme displays the sensing mechanism and the variance in charge density in the GM channel (Figure 5a). Gram-negative bacteria have a negative charge, and magainin I has many positive charges.[9] Therefore, the binding between magainin I and *E. coli* was mediated by the charge interaction, and the membrane of *E. coli* was immobilized on the magainin I-specific binding site shown in Figure 4c.[47,48] In addition, the charge carrier (hole) was collected in the channel of the MOGMFET after interaction with *E. coli* due to its negative charge. Therefore, the current was positively increased depending on the interaction amount of *E. coli.* To confirm the detection performance of the MOGMFET, the side-gated FET system was developed by MEMS technology, which carried out real-time measurements of *E. coli* exposure depending on the concentration (Figure 5b). An increased current level of the MOGMFET was observed with increasing concentration, which shows the different current change ratios. The normalized current variance was established by the following equation [Eq. (2)]:

$$\Delta I/I_0 = (I - I_0)/I_0 \tag{2}$$

where I and I_0 indicate the immediately current change after the exposure of target bacteria and the stable current level before exposure. To measure the reactivity, buffer injection was performed as a control experiment, which showed no significant signal, and then the cultured live *E. coli* was injected into the MOGMFET. The MOGMFET was exposed to various concentrations from 10^0 to 10^4 cfu mL^{-1}, and the variance in the current level was observed at 10^0 cfu mL^{-1} and showed a dynamic range from 10^0 to 10^3 cfu mL^{-1}. The LODs were 10^0 cfu mL^{-1}, and the detection time was observed to be ca. 10 s (Figure S7).

Moreover, the activity depending on the direction of magainin I was compared with the N-terminus-based MOGMFET, which presented lower sensitivity than the C-terminus MOGMFET. The positively charged amino acids of Magainin I as α-helical antimicrobial peptides are interacted via electrostatic attraction with the negatively charged phospholipids of the membrane of *E. coli.* However, the decreased sensitivity exhibited the interference influence by the residues of the including amine of the N-terminus surroundings.[44,47–49] The OGMFET showed no significant electrical signal after exposure to *E. coli.* Based on the results, the concentration curves were obtained by normalizing the sensitivity from Figure 5b (Figure 5c). The K values were calculated based on the Langmuir isotherm equation [Eq. (3)]:[50]

$$N = C/(1/K + C) \tag{3}$$

The binding affinities were 5.256×10^{-3} mL cfu^{-1} and 2.503×10^{-3} mL cfu^{-1} for the C–MOGMFET and N-MOGMFET, and the C-MOGMFET was confirmed to have a 2-fold higher binding affinity than the N-MOGMFET. To investigate the specific detection, *S. aureus* and *E. faecium* were exposed to the OGMFET and MOGMFET (Figure 5d). The OGMFETs showed no response toward any bacteria, and the MOGMFETs exhibited no response toward Gram-positive bacteria at 10^3 cfu mL^{-1}. *E. coli* at 10^0 cfu mL^{-1} was detected by the C-MOGMFET, and this platform showed excellent selectivity toward interference from different bacteria. In addition, the performance of the repeatability and the reproducibility were evaluated toward C-MOGM-

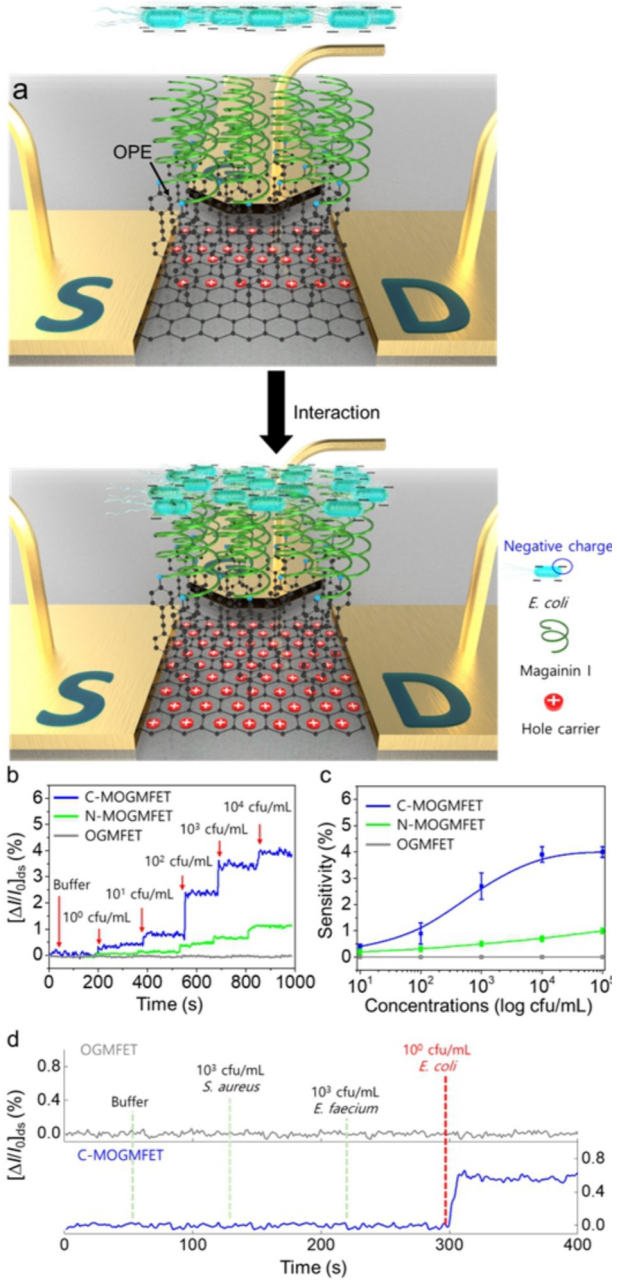

Figure 5. a) Illustration of the interaction mechanism between magainin I and *E. coli.* b) Real-time responses to various concentrations of *E. coli* in the C-MOGMFET, N-MOGMFET, and OGMFET. c) Calibration curves of the C-MOGMFET, N-MOGMFET, and OGMFET. d) Specificity of the C-MOGMFET and OGMFET toward nontarget bacteria (Gram-positive bacteria; *S. aureus* and *E. faecium*) and target bacteria (Gram-negative bacteria; *E. coli*).

© 2022 The Authors. Angewandte Chemie International Edition published by Wiley-VCH GmbH

FET using each bacterium over 5 times. The results exhibited high-selectivity, high-repeatability (Figure S8).

Conclusion

In summary, we synthesized a novel interface, OPE, including a functional group for covalent bonding on graphene, and successfully performed biosensor applications. The perfect covalent bonding between OPE and graphene was confirmed using surface and electrical analysis; in particular, the SAMs of OPE on graphene were clearly observed by TEM. In addition, the higher stable binding energy of OPE than other OICs was investigated using DFT simulation. Based on the results, the MEMS process was directly carried out for the fabrication of the OGM electrode, and magainin I as a bioprobe was clearly conjugated using an amide bond with an amine group of OPE. The clinical samples were exposed to MOGMFET, and these performances showed high sensitivity of 10^0 cfu mL^{-1} LOD toward the target clinical sample and high selectivity toward other clinical nontarget samples. Therefore, OPE compounds can be provided for the comfortable modification of graphene for biosensor applications.

Acknowledgements

This work was supported by Korea Institute of Planning and Evaluation for Technology in Food, Agriculture and Forestry (IPET) and Korea Smart Farm R&D Foundation (KosFarm) through Smart Farm Innovation Technology Development Program, funded by Ministry of Agriculture, Food and Rural Affairs (MAFRA) and Ministry of Science and ICT (MSIT), Rural Development Administration (RDA) (421020-03); the National Research Council of Science & Technology (NST) grant by the Korea government (MSIT) (No. CAP22011-000); Korea Ministry of Environment (MOE) through Technology Development Project for Safety Management of Household Chemical Products Program, funded by Korea Ministry of Environment (MOE) (2022002980005, 1485018893); National R&D Program of National Research Foundation of Korea (NRF) funded by Ministry of Science and ICT (NRF-2021M3H4A4079381); Nanomedical Devices Development Project of NNFC; the Korea Research Institute of Bioscience and Biotechnology (KRIBB) Research Initiative Program (KGM2112234).

Conflict of Interest

The authors declare no conflict of interest.

Data Availability Statement

The data that support the findings of this study are available in the supplementary material of this article.

Keywords: Biosensors · Covalent Bonding · Density Functional Theory · Interfacial Compounds · Oligo(Phenylene Ethynylene)

[1] O. S. Kwon, H. S. Song, T. H. Park, J. Jang, *Chem. Rev.* **2019**, *119*, 36–93.
[2] A. K. Geim, K. S. Novoselov, *Nat. Mater.* **2007**, *6*, 183–191.
[3] A. K. Geim, *Science* **2009**, *324*, 1530–1534.
[4] M. D. Esrafili, N. Saeidi, *New J. Chem.* **2017**, *41*, 13149–13155.
[5] L. A. Ponomarenko, F. Schedin, M. I. Katsnelson, R. Yang, E. W. Hill, K. S. Novoselov, A. K. Geim, *Science* **2008**, *320*, 356–358.
[6] C. Lee, X. Wei, J. W. Kysar, J. Hone, *Science* **2008**, *321*, 385–388.
[7] S. Chae, T. H. Le, C. S. Park, Y. Choi, S. Kim, U. Lee, E. Heo, H. Lee, Y. A. Kim, O. S. Kwon, H. Yoon, *Nanoscale* **2020**, *12*, 13351–13359.
[8] G. Seo, G. Lee, M. J. Kim, S. H. Baek, M. Choi, K. B. Ku, C. S. Lee, S. Jun, D. Park, H. G. Kim, S. J. Kim, J. O. Lee, B. T. Kim, E. C. Park, S. Il Kim, *ACS Nano* **2020**, *14*, 5135–5142.
[9] G. Wu, Z. Dai, X. Tang, Z. Lin, P. K. Lo, M. Meyyappan, K. W. C. Lai, *Adv. Healthcare Mater.* **2017**, *6*, 1700736.
[10] R. Hajian, S. Balderston, T. Tran, T. DeBoer, J. Etienne, M. Sandhu, N. A. Wauford, J.-Y. Chung, J. Nokes, M. Athaiya, J. Paredes, R. Peytavi, B. Goldsmith, N. Murthy, I. M. Conboy, K. Aran, *Nat. Biomed. Eng.* **2019**, *3*, 427–437.
[11] S. Sheibani, L. Capua, S. Kamaei, S. S. A. Akbari, J. Zhang, H. Guerin, A. M. Ionescu, *Commun. Mater.* **2021**, *2*, 10.
[12] X. Wang, Z. Hao, T. R. Olsen, W. Zhang, Q. Lin, *Nanoscale* **2019**, *11*, 12573–12581.
[13] S. Nazir, O. S. Kwon, *Appl. Sci. Converg. Technol.* **2022**, *31*, 40–45.
[14] Z. Li, Z. Liu, H. Sun, C. Gao, *Chem. Rev.* **2015**, *115*, 7046–7117.
[15] J. Park, M. Yan, *Acc. Chem. Res.* **2013**, *46*, 181–189.
[16] J. J. Stapleton, P. Harder, T. A. Daniel, M. D. Reinard, Y. Yao, D. W. Price, J. M. Tour, D. L. Allara, *Langmuir* **2003**, *19*, 8245–8255.
[17] S. UrRehman, M. Anwer, S. BiBi, S. Jamil, M. Yasin, S. Rauf Khan, R. Nadeem, S. Ali, R. Jia, *Mater. Sci. Semicond. Process.* **2022**, *140*, 106381.
[18] D. Jose, A. Datta, *Acc. Chem. Res.* **2014**, *47*, 593–602.
[19] K. H. Kim, J. E. An, J.-S. Kim, J. Bae, O. S. Kwon, *Appl. Sci. Converg. Technol.* **2021**, *30*, 111–114.
[20] S. H. Lee, K. H. Kim, S. E. Seo, M. il Kim, S. J. Park, O. S. Kwon, *J. Ind. Eng. Chem.* **2020**, *83*, 29–34.
[21] G. Ke, D. Su, Y. Li, Y. Zhao, H. Wang, W. Liu, M. Li, Z. Yang, F. Xiao, Y. Yuan, F. Huang, F. Mo, P. Wang, X. Guo, *Sci. China Mater.* **2021**, *64*, 739–747.
[22] K. H. Kim, D. Moon, J. E. An, S. J. Park, S. E. Seo, S. Ha, J. Kim, K. Kim, S. Phyo, J. Lee, H.-Y. Kim, M. Kim, T. H. Park, H. S. Song, O. S. Kwon, *Biosens. Bioelectron.* **2022**, *215*, 114551.
[23] A. Aljoundi, I. Bjij, A. El Rashedy, M. E. S. Soliman, *Protein J.* **2020**, *39*, 97–105.
[24] Y. Shu, D. G. Truhlar, *J. Chem. Theory Comput.* **2020**, *16*, 4337–4350.
[25] B. Stadtmüller, S. Emmerich, D. Jungkenn, N. Haag, M. Rollinger, S. Eich, M. Maniraj, M. Aeschlimann, M. Cinchetti, S. Mathias, *Nat. Commun.* **2019**, *10*, 1470.
[26] L. Liu, Z. Shen, *Appl. Phys. Lett.* **2009**, *95*, 252104.
[27] J. Zhang, L. Song, M. Sist, K. Tolborg, B. B. Iversen, *Nat. Commun.* **2018**, *9*, 4716.
[28] A. Migliore, N. F. Polizzi, M. J. Therien, D. N. Beratan, *Chem. Rev.* **2014**, *114*, 3381–3465.
[29] I. Hatial, R. Mukherjee, K. Senapati, A. Basak, *Tetrahedron Lett.* **2015**, *56*, 4275–4279.

© 2022 The Authors. Angewandte Chemie International Edition published by Wiley-VCH GmbH

[30] A. Hu, S. Griesing, M. Rybachuk, Q. B. Lu, W. W. Duley, *J. Appl. Phys.* **2007**, *102*, 074311.
[31] K. Roodenko, M. Gensch, J. Rappich, K. Hinrichs, N. Esser, R. Hunger, *J. Phys. Chem. B* **2007**, *111*, 7541–7549.
[32] A. C. Ferrari, J. C. Meyer, V. Scardaci, C. Casiraghi, M. Lazzeri, F. Mauri, S. Piscanec, D. Jiang, K. S. Novoselov, S. Roth, A. K. Geim, *Phys. Rev. Lett.* **2006**, *97*, 187401.
[33] L. M. Malard, M. A. Pimenta, G. Dresselhaus, M. S. Dresselhaus, *Phys. Rep.* **2009**, *473*, 51–87.
[34] A. Dimiev, D. V. Kosynkin, A. Sinitskii, A. Slesarev, Z. Sun, J. M. Tour, *Science* **2011**, *331*, 1168–1172.
[35] S. Niyogi, E. Bekyarova, J. Hong, S. Khizroev, C. Berger, W. de Heer, R. C. Haddon, *J. Phys. Chem. Lett.* **2011**, *2*, 2487–2498.
[36] A. Mueller, M. G. Schwab, N. Encinas, D. Vollmer, H. Sachdev, K. Müllen, *Carbon* **2015**, *84*, 426–433.
[37] L. J. O'Driscoll, X. Wang, M. Jay, A. S. Batsanov, H. Sadeghi, C. J. Lambert, B. J. Robinson, M. R. Bryce, *Angew. Chem. Int. Ed.* **2020**, *59*, 882–889; *Angew. Chem.* **2020**, *132*, 892–899.
[38] J. Deng, M. Liu, F. Lin, Y. Zhang, Y. Liu, S. Yao, *Anal. Chim. Acta* **2013**, *767*, 59–65.
[39] M. Hayyan, A. Abo-Hamad, M. A. AlSaadi, M. A. Hashim, *Nanoscale Res. Lett.* **2015**, *10*, 324.
[40] K. H. Kim, S. H. Lee, S. E. Seo, J. Bae, S. J. Park, O. S. Kwon, *Micromachines* **2020**, *11*, 439.
[41] S. J. Park, J. Lee, S. E. Seo, K. H. Kim, C. S. Park, S. H. Lee, H. S. Ban, B. D. Lee, H. S. Song, J. Kim, C. S. Lee, J. Bae, O. S. Kwon, *Sci. Rep.* **2020**, *10*, 3772.
[42] R. E. W. Hancock, H.-G. Sahl, *Nat. Biotechnol.* **2006**, *24*, 1551–1557.
[43] A. Al-Ahmad, D. Laird, P. Zou, P. Tomakidi, T. Steinberg, K. Lienkamp, *PLoS One* **2013**, *8*, e73812.
[44] M. S. Mannoor, S. Zhang, A. J. Link, M. C. McAlpine, *Proc. Natl. Acad. Sci. USA* **2010**, *107*, 19207–19212.
[45] J. E. An, K. H. Kim, S. J. Park, S. E. Seo, J. Kim, S. Ha, J. Bae, O. S. Kwon, *ACS Sens.* **2022**, *7*, 99–108.
[46] K. H. Kim, S. J. Park, C. S. Park, S. E. Seo, J. Lee, J. Kim, S. H. Lee, S. Lee, J.-S. Kim, C.-M. Ryu, D. Yong, H. Yoon, H. S. Song, S. H. Lee, O. S. Kwon, *Biosens. Bioelectron.* **2020**, *167*, 112514.
[47] K. Matsuzaki, K. Sugishita, M. Harada, N. Fujii, K. Miyajima, *Biochim. Biophys. Acta Biomembr.* **1997**, *1327*, 119–130.
[48] M. R. Wenk, J. Seelig, *Biochemistry* **1998**, *37*, 3909–3916.
[49] K. Matsuzaki, O. Murase, K. Miyajima, *Biochemistry* **1995**, *34*, 12553–12559.
[50] O. S. Kwon, H. S. Song, S. J. Park, S. H. Lee, J. H. An, J. W. Park, H. Yang, H. Yoon, J. Bae, T. H. Park, J. Jang, *Nano Lett.* **2015**, *15*, 6559–6567.

Manuscript received: July 4, 2022
Accepted manuscript online: August 15, 2022
Version of record online: September 1, 2022

© 2022 The Authors. Angewandte Chemie International Edition published by Wiley-VCH GmbH